



CHORUS

This is the accepted manuscript made available via CHORUS. The article has been published as:

Optical evidence of an enhanced electronic effective mass in the anomalous $\text{Pb}_{1-x}\text{Ti}_x\text{Te}$ superconductor

A. Pal, M. Chinotti, L. Degiorgi, P. Walmsley, and I. R. Fisher

Phys. Rev. Materials **3**, 054801 — Published 8 May 2019

DOI: [10.1103/PhysRevMaterials.3.054801](https://doi.org/10.1103/PhysRevMaterials.3.054801)

Optical Evidence of an Enhanced Electronic Effective Mass in the Anomalous $\text{Pb}_{1-x}\text{Tl}_x\text{Te}$ Superconductor

A. Pal, M. Chinotti, and L. Degiorgi*

Laboratorium für Festkörperphysik, ETH - Zürich, 8093 Zürich, Switzerland

P. Walmsley and I.R. Fisher

Geballe Laboratory for Advanced Materials and Department of Applied Physics, Stanford University, Stanford CA 94305, USA

(Dated: April 4, 2019)

The narrow band-gap semiconductor PbTe exhibits a number of striking properties upon thallium (Tl)-doping, including the onset of superconductivity at temperatures T_c which are substantially higher than for materials with equivalent charge carrier concentration. Here, we provide a thorough optical investigation of $\text{Pb}_{1-x}\text{Tl}_x\text{Te}$ over a very broad spectral range and contrast its normal-state, complete excitation spectrum with the optical response of the non-superconducting analog Na-doped PbTe. We capture the relevant energy scales shaping their electronic structure and uncover the formation of an impurity band upon doping with Tl, which evolves into a resonant state for large doping. This implies a large density of states and an enhancement of the optical effective mass m^*/m_e of the itinerant charge carriers, which is stronger for Tl- than for Na-doping. Since the enhancement of m^*/m_e particularly occurs upon crossing a critical concentration x_c in Tl-doped PbTe for which $T_c \neq 0$, we advance its relevance for the onset of superconductivity.

PACS numbers:

I. INTRODUCTION

The thermoelectric material PbTe, besides providing an alternative for power generation and refrigeration^{1,2}, also presents a series of unusual and poorly understood low-temperature electronic properties when appropriately doped. Of particular relevance to the present work, Tl substitution yields a metallic state, with no carrier freeze out to the lowest temperatures, and a superconducting ground-state for concentrations $x > x_c \sim 0.3\%$. The critical temperature increases linearly with the concentration of Tl dopants, with maximum values ($T_c \sim 1.4 \text{ K}^3$) that are anomalously high for the given carrier density of about $10^{20} \text{ holes/cm}^3$ ^{3,4,5}. Significantly, Tl is the only dopant to cause superconductivity in this material, so, for example, the analogous case of hole doping via Na substitution does not lead to superconductivity down to the lowest investigated temperature. It has therefore been conjectured that the special nature of the Tl impurities plays a prominent role⁶⁻⁸.

The anomalous electronic properties of $\text{Pb}_{1-x}\text{Tl}_x\text{Te}$ have previously been discussed in the context of the well-known valence-skipping nature of Tl, such that only Tl^{1+} and Tl^{3+} are the stable electronic configuration in ionic compounds. Such a mixed valency was indeed recently established spectroscopically⁹. The precise role played by such a mixed valency with respect to the superconductivity is presently unknown, but one possibility that has been suggested is that quantum valence fluctuations might set the stage for an electronic pairing mechanism^{7,8}.

Closely related to the observation of mixed valency, recent experimental work¹⁰, based on a combination of magnetotransport measurements (Shubnikov de Haas oscillations and Hall coefficient), Angle Resolved Photoe-

mission Spectroscopy (ARPES), and density functional theory (DFT) calculations of the electronic structure, found that for Tl concentrations beyond x_c the Fermi energy (ϵ_F) coincides with resonant impurity states. DFT calculations further indicate that these states derive principally from Tl orbitals^{11,12}, in which case the formal valence of the Tl impurities varies between 1+ and 3+ if the states are filled or empty. Such states should lead to a large density of states (DOS) and a strong enhancement of the average carrier effective mass. These observations motivate a more detailed investigation of the wider electronic structure by probing the charge dynamics; this is the purpose of the present work. Our results suggest that heavy charge carriers located at the Fermi level are a central component of the anomalous superconducting ground-state found in this material.

II. EXPERIMENT

The Tl- and Na-doped PbTe single crystals were grown by an unseeded physical vapor transport method, by sealing in vacuum polycrystalline pieces of the already doped compound, with (or close to) the desired final stoichiometry^{5,10,13}. The determination of the Tl and Na concentration was performed by comparing the measured Hall number of any given sample against a previously established calibration curve as well as by electron microprobe analysis. Table I summarises the nominal doping content x and y for $\text{Pb}_{1-x}\text{Tl}_x\text{Te}$ and $\text{Pb}_{1-y}\text{Na}_y\text{Te}$, investigated in this study, along with their charge carrier concentrations (p_{Hall}) and Sommerfeld γ values from Hall and specific heat data, respectively^{10,13}. Even though we do not provide data at exactly the very same doping content (for both Tl- and Na-doped PbTe), the investi-

Tl-doping x (%)	p_{Hall} (cm^{-3})	γ ($\text{JK}^{-2}\text{mol}^{-1}$)
0	1.88×10^{18}	0.03×10^{-3}
0.15	1.67×10^{19}	0.08×10^{-3}
0.4	5.88×10^{19}	0.43×10^{-3}
1.1	8.77×10^{19}	0.7×10^{-3}
1.5	1.3×10^{20}	0.75×10^{-3}
Na-doping y (%)	p_{Hall} (cm^{-3})	γ ($\text{JK}^{-2}\text{mol}^{-1}$)
0.13	2×10^{19}	0.09×10^{-3}
0.26	4.1×10^{19}	0.15×10^{-3}
0.62	9.25×10^{19}	0.23×10^{-3}

TABLE I: Nominal doping content x and y , charge carrier concentrations p_{Hall} (measured at 4 K) and Sommerfeld γ values from Hall and specific heat data, respectively, of $\text{Pb}_{1-x}\text{Tl}_x\text{Te}$ and $\text{Pb}_{1-y}\text{Na}_y\text{Te}$ ^{10,13}.

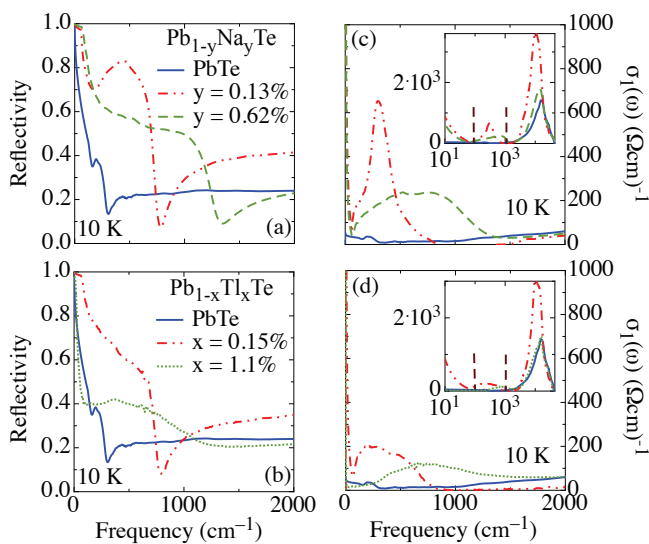


FIG. 1: (color online) (a,b) $R(\omega)$ and (c,d) $\sigma_1(\omega)$ at 10 K of representative Tl- and Na-doped PbTe compositions, respectively, compared to the spectra of the pristine PbTe compound. The insets in panels (c) and (d) display $\sigma_1(\omega)$ at 10 K for the same compositions up to $4 \times 10^4 \text{ cm}^{-1}$ (logarithmic energy scale). The vertical dashed lines in the insets mark the cut-off energy scales $\omega_c \sim 100$ and 1000 cm^{-1} (see text).

gated compositions cover the same range of charge carrier concentration after the Hall data.

We measure the temperature (T) dependence of the optical reflectivity $R(\omega)$ at nearly normal incidence with a Fourier-transform infrared interferometer (Bruker Vertex 80v), working in the spectral range from the far-infrared (FIR) up to the near-infrared (NIR), i.e. between 30 and 12000 cm^{-1} . This set of data is complemented at room temperature with those obtained by the PerkinElmer Lambda 950 from NIR up to the ultra-violet (UV) range, i.e. $4000\text{-}48000 \text{ cm}^{-1}$. For the purpose of the Kramers-Kronig (KK) transformation of $R(\omega)$, in order to access the optical functions, we perform the following appropriate extrapolations at high frequencies as well as

towards zero¹⁴; for $\omega \rightarrow 0$, we made use of the Hagen-Rubens formula ($R(\omega) = 1 - 2\sqrt{\frac{\omega}{\sigma_{dc}}}$), inserting the dc conductivity values (σ_{dc}) consistent with the relative T dependence of the transport data from Ref.¹⁵, and above the upper frequency limit we consider the extrapolation $R(\omega) \sim \omega^{-s}$ ($2 \leq s \leq 4$) in order to approach the electronic continuum¹⁴.

III. RESULTS AND DISCUSSION

Figures 1(a) and (b) display the measured reflectivity $R(\omega)$ at 10 K of representative Tl- and Na-compositions, compared to the spectra of the pristine PbTe compound. The T evolution of $R(\omega)$ is deployed for selected compounds in Fig. 4 in the Appendix. Some qualitative observations can be immediately made: the $R(\omega)$ spectrum of PbTe attests to a rather poor conducting material, as evinced by the low frequency onset of an extremely overdamped plasma edge and due to Pb vacancies creating holes in the valence band. For the pristine compound, there is also a broad feature at about 180 cm^{-1} that overlaps with the weak, vacancies-induced plasma edge. It is caused by a so-called mixed plasmon-phonon mode^{16,17}.

Doping PbTe by Na and Tl leads to a rather common evolution of the optical response with respect to the pristine compound, even though important nuances allow the differentiation of the absorption features of both investigated compositions. Upon doping we initially observe the formation of a rather sharp plasma edge in the measured $R(\omega)$ quantity (Fig. 1(a) and (b) and Fig. 4). For low Na-content that edge is overlapped by a strong additional FIR absorption at about 300 cm^{-1} . For low Tl-doping though, this latter feature is broader than for equivalent Na-compositions. The most remarkable change is observed at large doping, at which the plasma edge of $R(\omega)$ move towards higher frequencies. Upon doping, $R(\omega)$ also progressively gets overdamped, prior to a sharp increase of $R(\omega)$ at the lowest frequencies accessible by our experiment. This latter behaviour is more pronounced in Tl- than in Na-doped PbTe. This signals a stronger increase of the scattering in Tl-compositions than in Na-doped PbTe for the great majority of the doping-induced itinerant charge carriers. Conversely, a residual small fraction of the free charge carriers with long relaxation time seems to shape the charge dynamics at the lowest frequencies in both compositions. The FIR absorption feature at large doping is at most a broad shoulder overlapping with the plasma edge of $R(\omega)$ for both Na- and Tl-doped PbTe.

The resulting real part $\sigma_1(\omega)$ of the optical conductivity at 10 K is shown in panels (c) and (d) of Fig. 1 for selected compositions up to 2000 cm^{-1} . $\sigma_1(\omega)$ images the features recognised in $R(\omega)$ as the Drude resonance and the FIR absorption and their evolution upon doping. As elaborated in Fig. 5 in the Appendix, there is a rather monotonic T dependence of those features for each dop-

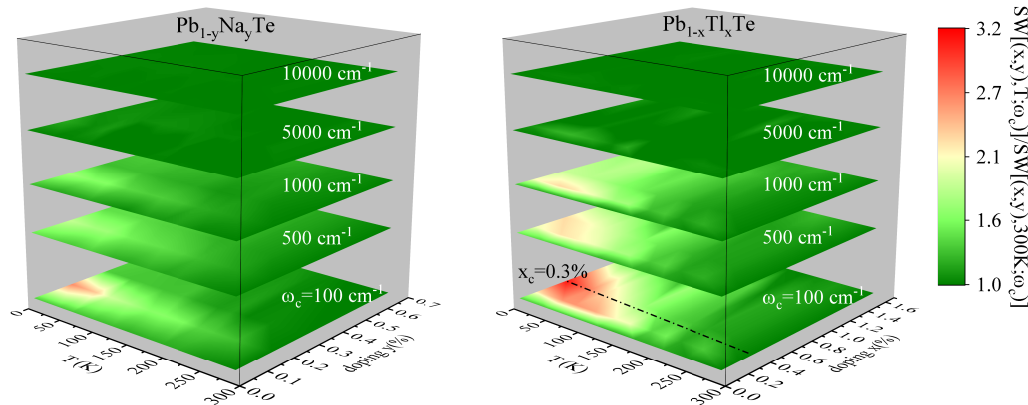


FIG. 2: (color online) T and doping content dependence of the integrated spectral weight SW (Eq. (1)) from zero up to the indicated cut-off frequency ω_c , normalised by its value at 300 K, for both PbTe compositions. A first-neighbor interpolation procedure is used in order to generate the color maps.

ing, mostly coinciding with their overall enhancement at low T . The charge dynamics for all compounds is dominated by the strong absorption peaked at about $\omega_0 \sim 10^4 \text{ cm}^{-1}$ and with a low frequency onset around 2000 cm^{-1} (insets of Fig. 1(c) and (d)). This feature is in broad agreement with previous optical investigations (see Ref. 18 for an ample literature), focusing the attention to the high frequency visible and UV spectral ranges and addressing the narrow-gap excitation, and can be well reproduced by first principle calculations¹⁸. The low frequency spectral range displays the metallic (but weak) Drude resonance, which is ascribed to the so-called coherent contribution of $\sigma_1(\omega)$. It generally appears upon doping and tends to further extend into a broad tail at higher frequencies, labeled as the incoherent component of $\sigma_1(\omega)$. For the Tl-doped PbTe at $x > x_c$ the coherent metallic term develops at rather low frequencies. The FIR mode shifts to higher frequencies with doping at all PbTe compositions and is overlapped to the incoherent metallic part of $\sigma_1(\omega)$. This latter absorption is quite sharp for low Na-doping while it broadens upon increasing the doping concentration (Fig. 1(c)). At variance for all Tl-compositions the FIR feature distributes over a broad energy interval in $\sigma_1(\omega)$ (Fig. 1(d)), as already pointed out above when describing the $R(\omega)$ spectra.

The impact of doping has been extensively studied both experimentally and theoretically, showing diverse effects as a function of dopant into the physical properties^{19–21}. It is generally recognized that the resulting optical response features so-called impurity energy states, which give rise to electronic interband transitions located in the FIR spectral range just above the metallic Drude resonance¹⁹. We may already anticipate the common notion^{19–21} that a pinning of ϵ_F to the impurity state occurs upon increasing the dopant concentration, although it depends from the dopant itself and its degree of hybridization with the valence band. The broadening of the FIR absorption feature with increased

doping content suggests that the impurity energy states are somewhat broadly distributed in energy.

We now turn our attention to the tools for the data analysis, with the main goal to extract from $\sigma_1(\omega)$ the concentration (n) and the effective mass (m^*/m_e) of the itinerant charge carriers. First of all, we introduce the well-established instrument of the integrated spectral weight, which is defined as the integral of $\sigma_1(\omega)$ up to a cut-off energy (ω_c):

$$SW(T; \omega_c) = \int_0^{\omega_c} \sigma_1(\omega, T) d\omega \quad (1)$$

This model-independent quantity conveys the number of the carriers, normalized by their effective mass, contributing to the optical processes up to ω_c . Therefore, in the $\omega_c \rightarrow \infty$ limit, it is expected to merge into a constant value at all T , satisfying the f -sum rule¹⁴. In our data, the full recovery of SW is achieved at energy scales of about 2 eV ($1.6 \times 10^4 \text{ cm}^{-1}$) for all compositions, well within the measurable spectral range and thus excluding reshuffling of SW among energy scales outside our experimental energy interval. Figure 2 displays the corresponding evolution of SW normalized by its value at 300 K as a function of T and doping content for different cut-off frequencies ω_c (for additional details we refer to Fig. 6 in the Appendix). We point out the astonishing accumulation of SW , to be addressed later, with respect to 300 K at FIR frequencies (i.e., $\omega_c \sim 100\text{--}500 \text{ cm}^{-1}$), principally occurring below $T^* \sim 100 \text{ K}$ and for Tl-compositions with $x \sim x_c$. For the purpose of our analysis we will exclusively consider the cut-off frequencies at 100 and 1000 cm^{-1} (see vertical marks in the insets of Fig. 1(c) and (d)). The first one identifies the range where the coherent part of $\sigma_1(\omega)$ (i.e., Drude resonance) expires, while the second one is at the end of the incoherent part of $\sigma_1(\omega)$ right at the onset of the narrow-gap absorption¹⁸.

In order to obtain both m^*/m_e and n , we must consider an additional constraint, given by the Sommerfeld γ value of the electronic specific heat, which necessarily encompasses all states at ϵ_F . From its definition we can evince the following expressions^{22,23} ($\omega_p = 2\pi\nu_p$):

$$\frac{m^*}{m_e} = \left(\frac{\gamma}{V_m}\right)^{3/4} \frac{1}{\sqrt{2\pi\nu_p}}, n = \left(\frac{\gamma}{V_m}\right)^{3/4} (2\pi\nu_p)^{3/2}, \quad (2)$$

where V_m is the molar volume²⁴. Both expressions obviously imply that $\gamma \sim (3\pi^2 n)^{1/3} m^* V_m$. The integrated $SW(\omega_c)$ of Eq. (1) can be understood as an oscillator strength, which would be proportional to the squared plasma frequency $\omega_p^2 = \frac{4\pi e^2 n}{m^*}$ of the metallic-like, coherent (Drude) contribution when $\omega_c = 100 \text{ cm}^{-1}$ or of the total coherent and incoherent components in $\sigma_1(\omega)$ when $\omega_c = 1000 \text{ cm}^{-1}$. We can then plug into Eqs. (2) the integrated spectral weight $SW(\omega_c)$ for ω_p^2 , together with the measured Sommerfeld γ values (Table I).

Figure 3 summarises the outcome of this analysis, showing the resulting m^*/m_e and n as a function of the doping content. The effective mass for Tl-doped PbTe is more strongly enhanced upon crossing x_c than for any Na-doped compositions. This is particularly emphasised for the estimation of m^*/m_e at $\omega_c = 100 \text{ cm}^{-1}$ which possibly represents the true mass enhancement of the itinerant charge carriers located in the (coherent) Drude-like resonance. In the Appendix we elaborate further on the relationship between m^*/m_e and n : from the representation $m^* \sim n^{-1/3}$, as expected from Eqs. (2), and by imposing $n = p_{Hall}$ we can also confirm that $m_{Tl}^* > m_{Na}^*$ for increasing doping content (Fig. 7). This latter representation of our data analysis emphasises the robustness of the mass enhancement for the Tl compositions with equivalent p_{Hall} than the Na-ones. While the definition of the effective mass depends very much from the performed experiment²⁶, we note a fair agreement as far as the overall trend is concerned between our optical effective mass (Fig. 3(a) and (b)) and the cyclotron mass determined from the Shubnikov de Haas oscillations' amplitude (Fig. S7 in the Supplemental Material of Ref. 10).

The extracted charge carrier concentration n up to $\omega_c \sim 100 \text{ cm}^{-1}$ for both PbTe compositions is quite small, particularly for large doping content (i.e., exceeding x_c for Tl-doped PbTe), with respect to the measured p_{Hall} , which is also shown as comparison in Fig. 3(c) and (d). This means that just a fraction of the charge carrier concentration, introduced by doping, is encountered in the coherent component (i.e., effective Drude-like resonance) of $\sigma_1(\omega)$. In this respect and interestingly enough, our estimation of n after Eq. (2) does coincide fairly well with p_{Hall} , when $\sigma_1(\omega)$ is integrated up to $\omega_c \sim 1000 \text{ cm}^{-1}$. This anticipates the idea (see below) that the conduction band in Tl- as well as Na-doped PbTe results from hole-doping of the valence band (most probably at the L -point of the Brillouin zone (BZ)) and that a great por-

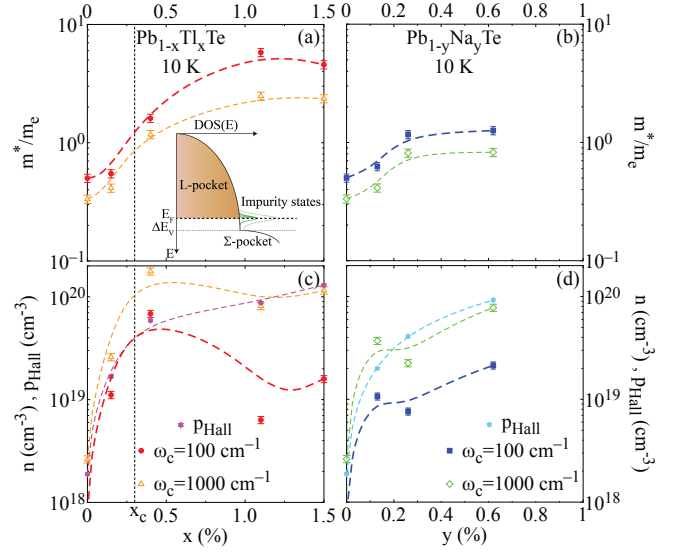


FIG. 3: (color online) Optical mass m^*/m_e and charge carrier concentration n as a function of the doping content in $\text{Pb}_{1-x}\text{Tl}_x\text{Te}$ (a,c) and $\text{Pb}_{1-y}\text{Na}_y\text{Te}$ (b,d), estimated from Eqs. (1) and (2) (see text) at 10 K and for both $\omega_c \sim 100$ and 1000 cm^{-1} . The measured p_{Hall} values (Table I) from Hall data are shown as comparison. The vertical thin dashed line in panel (a) and (c) marks $x_c \sim 0.3\%$. The dashed lines in all panels are spline data interpolations as a guide to the eyes. The scheme in panel (a) sketches the DOS proposed in Ref. 10.

tion of the charge carriers contributes to the incoherent component of $\sigma_1(\omega)$.

The key players in the electronic structure of PbTe are the valence bands at the L - and Σ -points of the BZ^{10,13}. ARPES investigations for Tl-compositions below and above x_c definitely rule out the presence at ϵ_F of the Σ -pocket¹⁰. In non-superconducting Na-doped PbTe the Luttinger volume of the L -pocket and the Hall number are in excellent agreement for all compositions, indicating that all mobile charges are contained within the L -pocket¹³. However, the Hall number in Tl-doped PbTe falls below the expected value if each Tl dopant were to contribute a single hole (as expected for a Tl^{1+} valence), but still gives a significantly higher estimate of the carrier concentration than the L -pocket Luttinger volume, for composition exceeding x_c ¹⁰. It is natural to conclude that in Tl-doped PbTe there must be additional mobile states outside of the L -pocket, located within a relatively narrow band at ϵ_F and resonating with the L -pocket itself. This immediately leads to DOS in the inset of Fig. 3(a), as first proposed by Ref. 10.

The formation of the resonant band at ϵ_F might be very much associated with the valence skipper property of the Tl ion and its origin could be related to the scenario based on the charge Kondo model⁷, as originally advanced by *dc* transport data⁵. However, since the impurity levels are somewhat broadened in energy, the best picture to have in mind is that of virtual bound states.

In such a picture, the width of the resonant states, having predominantly Tl character, is controlled first by the hybridization with the PbTe bands (mostly L band), and second by the overlap with nearby impurity states. ϵ_F lies close or within the resonant impurity band, which is centered below the top of the valence band and can contribute to the conductivity.

Our findings corroborate these latter notions. Although $\sigma_1(\omega)$ in both PbTe compositions may be commonly addressed within the proposed DOS (inset of Fig. 3(a)¹⁰), its consequences for the optical response are more pertinent for the Tl-doped PbTe. First of all, the resulting metallic $\sigma_1(\omega)$ after the sketched DOS will encounter a coherent as well as incoherent component which tend to be distinct upon increasing the doping content. One could state that in doped PbTe the itinerant carriers are somehow localised on the short and delocalised on the long wave length limit. The fraction of carriers located within the DOS resonance pinned at ϵ_F are characterised by a large effective mass, which turns out to be strongly enhanced in Tl-doped PbTe compositions for $x > x_c$ rather than in $\text{Pb}_{1-y}\text{Na}_y\text{Te}$ (Fig. 3(a) and (b)). The second generic optical feature is the FIR absorption originating from the impurity states, which is quite sharp at low doping content. This excitation then transforms into a broader absorption, located at higher energies upon increasing the doping concentration, when the hybridisation of the impurity level with the valence band takes place. That broad absorption at 1000 cm^{-1} , which overlaps the incoherent contribution to $\sigma_1(\omega)$, basically stems from excitations between the states with (mainly) Σ -band character and the impurity band pinned at ϵ_F . In fact, the relative difference between the top of the L and Σ band ranges between 130 and 200 meV in PbTe, as revealed in ARPES^{10,27}. With doping this energy scale should get smaller, thus being comparable to and consistent with the frequency range of our (broad) FIR absorption.

Even though we focus here our attention on the data at 10 K, it is worthwhile to briefly comment on the T dependence of the optical response. The latter is particularly subtle in terms of the relative SW reshuffling with respect to 300 K (Fig. 2). Interestingly enough our characteristic temperature T^* coincides with $T_K \sim 50\text{-}70\text{ K}$ extracted from thermoelectric power (TEP)²⁸ in $\text{Pb}_{1-x}\text{Tl}_x\text{Te}$ ($0 \leq x \leq 1.3\%$) after concepts based on the physics of dilute magnetic alloys. To which extent such a Kondo-like physics (e.g., charge-Kondo scenario^{7,8}) is pertinent to the title compound is beyond the scope of our work and it is generally highly debated. Already the variation by almost a factor of ten in the estimation of T_K between transport properties ($T_K \sim 5\text{ K}$)⁵ and TEP²⁸ is indicative of the limitations of such a scenario. Here, we wish to highlight the necessity to reach low enough T (i.e., $< T^*$ for $x \sim x_c$), so that the thermal broadening $k_B T$ is smaller than the width (Γ) of the resonant band pinned at ϵ_F , a prerequisite in order to resolve it. Therefore, we propose $\Gamma \sim k_B T^*$ as the relevant energy scale

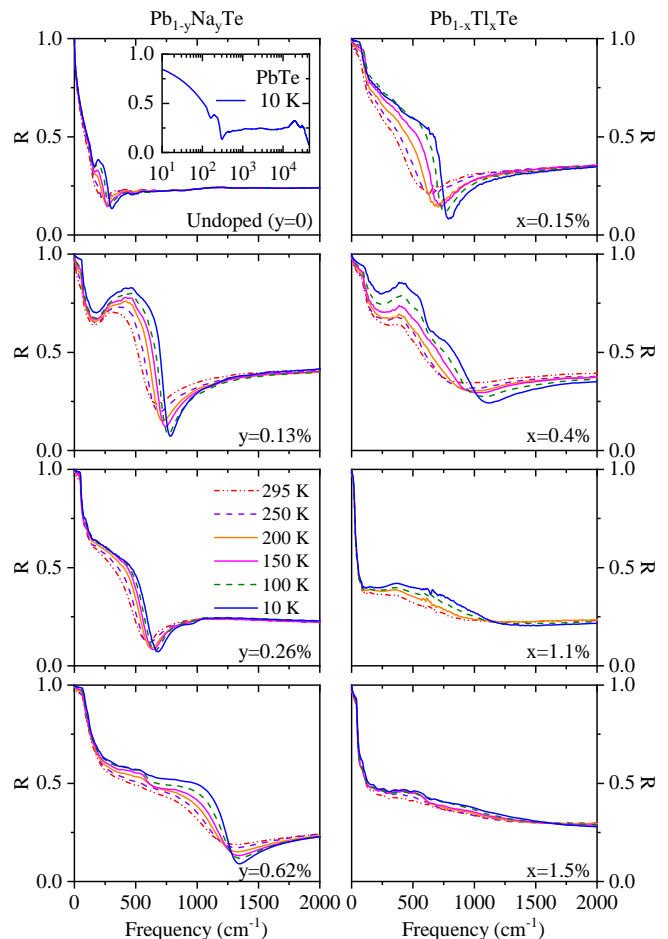


FIG. 4: (color online) Reflectivity ($R(\omega)$) spectra of representative (left) Na- and (right) Tl-doped PbTe as a function of T and up to 2000 cm^{-1} . The inset emphasises $R(\omega)$ of PbTe at 10 K in the whole spectral range (logarithmic scale). The same color and line code for the T legend applies to all panels.

in Tl-doped PbTe at least for $x \sim x_c$. Upon increasing x beyond x_c , Γ is already substantially larger than the thermal broadening at 300 K, so that upon lowering T the relative change of SW with respect to 300 K is less pronounced and tends then to disappear.

IV. CONCLUSION

Even though the overall optical response for both Na- and Tl-doped PbTe shares rather common, similar features, it clearly emerges from our investigation, that the effective optical mass m^*/m_e is the key quantity somehow discriminating between the two investigated PbTe compositions. We provide evidence for a strong enhancement of the optical effective mass in $\text{Pb}_{1-x}\text{Tl}_x\text{Te}$ for $x > x_c$ than in $\text{Pb}_{1-y}\text{Na}_y\text{Te}$. Our results advance in principle the intriguing possibility that superconductivity may be the consequence of the pairing of 'heavy' quasi-particles associated to charged valence-states⁹.

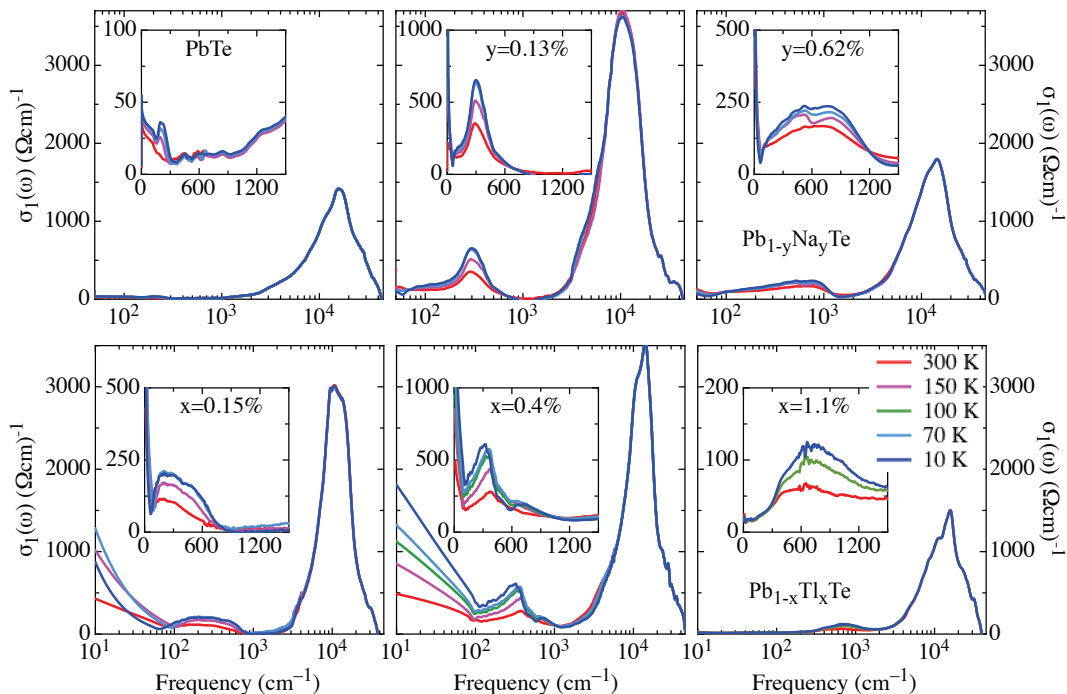


FIG. 5: (color online) Real part $\sigma_1(\omega)$ of the optical conductivity of representatives Na- (upper row) and Tl-doped PbTe (lower row) at selected T . The insets emphasise the T dependence of the FIR absorption feature (see main paper).

Appendix

A. Additional Data and Analysis

1. Optical reflectivity and conductivity

Complementary to the data reported in the main paper, we review here in Fig. 4 the T dependence of the measured $R(\omega)$ up to 2000 cm^{-1} for representative compositions of Tl- and Na-doped PbTe. The spectra at high frequencies for both compositions do coincide with $R(\omega)$ of PbTe, shown in the inset at 10 K and in the whole spectral range. This also means that we could apply above 48000 cm^{-1} the same extrapolation procedure at all compositions for the KK transformation. This strengthens the reliability of our $R(\omega)$ data and extracted $\sigma_1(\omega)$ below 5000 cm^{-1} , where the main discussion is developed and the major conclusions of our work emerges.

Even a small concentration of Pb or Te vacancies in PbTe leads to metallic behaviour. In our case, due to the synthesis conditions/methods that we employ, it is Pb vacancies. The large dielectric constant of PbTe screens the resulting impurity potential very effectively, and the holes do not freeze out to the lowest T (i.e., they form a Fermi surface).

We can reiterate and emphasise the progressively enhanced optical metallicity (i.e., the appearance of the plasma edge in $R(\omega)$) upon doping. The onset of the plasma edge gets sharper (particularly at low doping concentrations for both PbTe compositions) and the edge it-

self tends to undergo a blue-shift upon lowering T . Once again, we wish to note the more strongly overdamped behaviour of $R(\omega)$ at all T for high Tl-doping. The metallic behaviour of $R(\omega)$ results in a Drude component of the real part $\sigma_1(\omega)$ of the optical conductivity (Fig. 5), which becomes narrower upon lowering T at any doping concentration x or y . As anticipated in the main paper, we recall again that at large doping the so-called incoherent component of $\sigma_1(\omega)$ tends to dominate over the small coherent part developing at low frequencies. We also observe a FIR absorption at about 300 cm^{-1} , which is narrower at low doping content for the Na-doped than for Tl-doped PbTe (insets of Fig. 5). Upon increasing the doping content such a feature gets broader in Na-doped PbTe compounds and shifts to higher frequencies for both PbTe compositions. That FIR absorption is enhanced upon lowering T in Na- and Tl-doped PbTe.

2. Spectral weight reshuffling

The integrated spectral weight SW , defined in Eq. (1), is a key quantity in our proposed data analysis. Here, we further elaborate on its distribution and reshuffling as a function of T and doping content. In addition to Fig. 2, one can consider the spectral weight normalized to 300 K encountered in $\sigma_1(\omega)$ between 100 and 1000 cm^{-1} (vertical dashed lines in the insets of Fig. 1(c) and (d)), as shown in Fig. 6. This quantity (SW_{100}^{1000}) is related to the energy interval of the high frequency Drude tail and

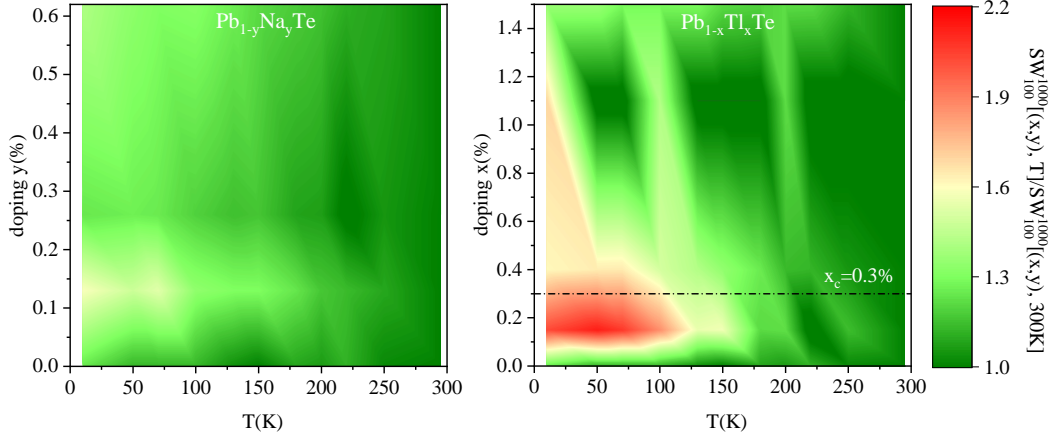


FIG. 6: (color online) T and doping content dependence of the integrated spectral weight (SW_{100}^{1000} , after Eq. (1)) between 100 and 1000 cm^{-1} (vertical dashed lines in the insets of Fig. 1(c) and (d)), normalised by the same quantity at 300 K, for both PbTe compositions. A first-neighbor interpolation procedure is used in order to generate the color maps.

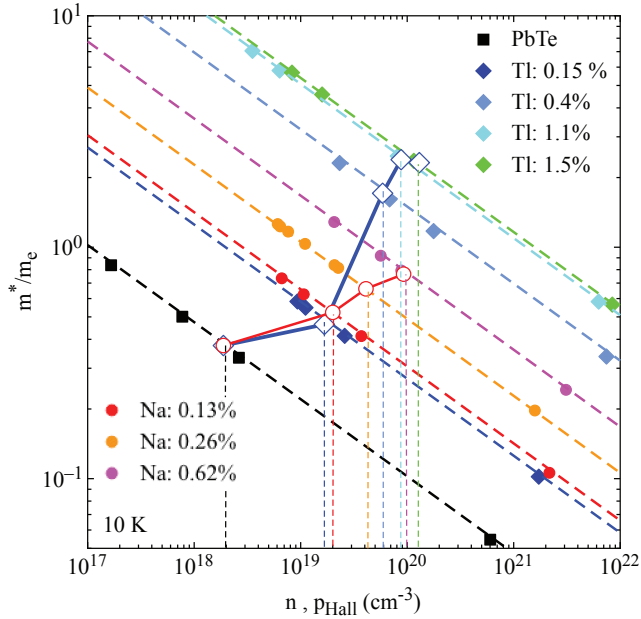


FIG. 7: (color online) Effective mass m^*/m_e versus charge carrier concentration n as estimated from Eqs. (2) for both sets of $\text{Pb}_{1-x}\text{Tl}_x\text{Te}$ and $\text{Pb}_{1-y}\text{Na}_y\text{Te}$ compositions at 10 K. It is an alternative and extended representation of our data in Fig. 3, where the doping concentration x or y is here an implicit variable. Each pair of m^*/m_e and n corresponds to their estimation when considering SW at different ω_c as input for Eqs. (2). SW was calculated for $\omega_c = 10, 100, 1000$ and $4 \cdot 10^4 \text{ cm}^{-1}$. The dashed lines emphasise the expected relationship $m^* \sim n^{-1/3}$, implicit in Eqs. (2). The vertical thin dashed lines (with the same color code as for the different doping content) identify the measured p_{Hall} (Table I). The thick color lines join the resulting m^*/m_e (blue open diamond and red open circle for Tl- and Na-doped PbTe, respectively) at the intercept of p_{Hall} with the $m^* \sim n^{-1/3}$ curves.

incoherent (metallic) contribution as well as the impu-

urity mode. Also from this perspective, one can evince a stronger enhancement of SW_{100}^{1000} with respect to 300 K for Tl-doped PbTe at doping content around x_c than for any Na-doped PbTe, which particularly develops at $T < 100$ K. As discussed in the main paper, this signals the interplay between the Tl content x , the width of the resulting impurity band and the thermal energy scale $k_B T$.

It is worth mentioning that a new phonon mode appears in pure PbTe with increasing $T > 100$ K, which is accompanied by a giant anharmonic phonon scattering^{29,30}. This implies a reshuffling of SW , which however gets enhanced well above room temperature. Such a reshuffling involving phonon modes is generally expected to be rather tiny and moreover in this case it is obviously opposite as a function of T than in our findings. These arguments indicate that this can not be the most relevant mechanism for the SW redistribution observed in our spectra (Fig. 2 and 6).

B. Alternative view on the optical effective mass versus charge carrier concentration

Figure 7 displays the effective mass m^*/m_e versus the charge carrier concentration n as estimated from Eqs. (2) when inserting for ω_p^2 the integrated spectral weight (Eq. (1)) up to selected ω_c (see Figure caption) for both sets of Tl- and Na-doped PbTe compositions at 10 K. As implicit in Eqs. (2) themselves, all entries satisfy the relationship $m^* \sim n^{-1/3}$. The purpose of this representation is in order to iterate that in Tl-doped PbTe the enhancement of the optical effective mass upon increasing x is more substantial than in any Na-doped compositions. For instance, one can observe how m^*/m_e behaves as a function of doping when taking $n = p_{Hall}$. At such p_{Hall} values (vertical thin dashed lines in Fig. 7) the enhancement of m^*/m_e is in fact more pronounced in Tl- than in Na-doped PbTe.

Acknowledgements

The authors wish to thank P. Giraldo-Gallo for crystal growth as well as N. Spaldin and T. Weber for fruitful discussions. This work was supported by the Swiss National Science Foundation (SNSF). Work at Stanford was supported by AFOSR Grant No. FA9550-09-1-0583.

* Correspondence and requests for materials should be addressed to: L. Degiorgi, Laboratorium für Festkörperphysik, ETH - Zürich, 8093 Zürich, Switzerland; email: degiorgi@solid.phys.ethz.ch.

-
- ¹ X. Zhang and L. D. Zhao, *J. Mater.* **1**, 92 (2015).
² Y. Xiao and L. D. Zhao, *npj Quantum Mater.* **3**, 55 (2018).
³ Y. Matsushita, P. A. Wiancki, A. T. Sommer, T.H. Geballe, and I. R. Fisher, *Phys. Rev. B* **74**, 134512 (2006).
⁴ I. A. Chernik and S. N. Lykov, *Sov. Phys. Solid State.* **23**, 2956 (1981).
⁵ Y. Matsushita, H. Bluhm, T. H. Geballe, and I. R. Fisher, *Phys. Rev. Lett.* **94**, 157002 (2005).
⁶ T. A. Costi and V. Zlatič, *Phys. Rev. Lett.* **108**, 036402 (2012).
⁷ M. Dzero and J. Schmalian, *Phys. Rev. Lett.* **94**, 157003 (2005).
⁸ J. E. Hirsch and D. J. Scalapino, *Phys. Rev. B* **32**, 5639 (1985).
⁹ P. Walmsley, C. Liu, A. D. Palczewski, P. Giraldo-Gallo, C. G. Olson, I. R. Fisher, and A. Kaminski, *Phys. Rev. B* **98**, 184506 (2018).
¹⁰ P. Giraldo-Gallo, P. Walmsley, B. Sangiorgio, S. C. Riggs, R. D. McDonald, L. Buchauer, B. Fauqué, C. Liu, N. A. Spaldin, A. Kaminski, K. Behnia, and I. R. Fisher, *Phys. Rev. Lett.* **121**, 207001 (2018).
¹¹ S. Ahmad, S. D. Mahanti, K. Hoang, and M. G. Kanatzidis, *Phys. Rev. B* **74**, 155205 (2006).
¹² K. Xiong, G. Lee, R. P. Gupta, W. Wang, B. E. Gnade, and K. Cho, *J. Phys. D.* **43**, 405403 (2010).
¹³ P. Giraldo-Gallo, B. Sangiorgio, P. Walmsley, H. J. Silverstein, M. Fechner, S. C. Riggs, T. H. Geballe, N. A. Spaldin, and I. R. Fisher, *Phys. Rev. B* **94**, 195141 (2016).
¹⁴ M. Dressel and G. Grüner *Electrodynamics of Solids*, Cambridge University Press, Cambridge, England (2002).
¹⁵ Y. Matsushita, *PhD. Thesis*, Stanford University, USA (2007), private communication.
¹⁶ A. I. Belogorokhov, L. I. Belogorokhova, D. R. Khokhlov, and S. V. Lemesheko, *Semiconductors* **36**, 663 (2002).
¹⁷ We do not observe the predicted single IR-active T_{1u} phonon, which anyhow is expected below 1 THz (M. Tani, R. Fukasawa, H. Abe, S. Matsuura, K. Sakai, and S. Nakashima, *J. Appl. Phys.* **83**, 2473 (1998)) and is totally screened by the (enhanced) metallic contribution to the optical response upon increasing the doping concentration.
¹⁸ C. E. Ekuma, D. J. Singh, J. Moreno, and M. Jarrell, *Phys. Rev. B* **85**, 085205 (2012).
¹⁹ M. V. Nikolic, K. M. Paraskevopoulos, T. Iveti, T. T. Zorba, S. S. Vujatovic, E. Pavlidou, V. Blagojevic, A. Bojicic, O. S. Aleksic, N. Nikolic, W. Knig, and P. M. Nikolic, *J. Mater. Sci.* **45**, 5910 (2010).
²⁰ K. Hoang, S. D. Mahanti, and P. Jena, *Phys. Rev. B* **76**, 115432 (2007).
²¹ I. I. Ivanchik, D. R. Khokhlov, A. V. Morozov, A. A. Terekhov, E. I. Slynko, V. I. Slynko, A. de Visser, and W. D. Dobrowolski, *Phys. Rev. B* **61**, R14889 (2000).
²² N. W. Ashcroft and N. D. Mermin *Solid State Physics*, Holt-Saunders Int. Editions, Philadelphia (1976).
²³ L. Degiorgi, *Rev. Mod. Phys.* **71**, 687 (1999) and references therein.
²⁴ The molar volume of PbTe is equal to $40.48 \times 10^{-6} \text{ m}^3/\text{mole}$ and it has been considered equivalent for both Na- and Tl-PbTe compositions.
²⁵ The integration of $\sigma_1(\omega)$ up to 1000 cm^{-1} encounters a fraction of SW due to the excitation originating from the impurity energy state. Nonetheless, we adopt here a SW analysis, which neglects an *ad-hoc* subtraction from the total SW of that contribution. This latter simplification may lead to an underestimation of m^*/m_e and an overestimation of n , particularly at low Na-doping content, for which the FIR absorption is narrow and strong. Nevertheless, we are convinced that the overall conclusions of our work across several doping contents are not severely affected by our simplified SW procedure.
²⁶ J. Merino and R. H. McKenzie, *Phys. Rev. B* **62**, 2416 (2000).
²⁷ J. Zhao, C. D. Malliakas, D. Bugaris, N. Appathurai, V. Karlapati, D. Y. Chung, M. G. Kanatzidis, and U. Chatterjee, <http://arxiv.org/Abs/1404.1807> (2014).
²⁸ M. Matusiak, E. M. Tunncliffe, J. R. Cooper, Y. Matsushita, and I. R. Fisher, *Phys. Rev. B* **80**, R220403 (2009).
²⁹ O. Delaire, J. Ma, K. Marty, A. F. May, M. A. McGuire, M.-H. Du, D. J. Singh, A. Podlesnyak, G. Ehlers, M. D. Lumsden, and B. C. Sales, *Nat. Mater.* **10**, 614 (2011).
³⁰ K. M. Ø. Jensen, E. S. Bozin, C. D. Malliakas, M. B. Stone, M. D. Lumsden, M. G. Kanatzidis, S. M. Shapiro, and S. J. L. Billinge, *Phys. Rev. B* **86**, 085313 (2012).